metals

MDPI

Article

High–Strength Porous TiNbZrTaFe Alloys Fabricated by Sintering of Nanocomposite Powder Precursor with Space Holder Technique

Yuhua Li [1,*], Yuxin He [1], Rong Zhao [1], Libin Niu [1], Juxin Qu [2] and Lai-Chang Zhang [3,*]

[1] College of Mechanical Engineering, Xi'an University of Science and Technology, Xi'an 710054, China
[2] National Engineering Research Center of Near–Net–Shape Forming for Metallic Materials, South China University of Technology, Guangzhou 510640, China
[3] School of Engineering, Edith Cowan University, 270 Joondalup Drive, Joondalup, Perth, WA 6027, Australia
* Correspondence: liyuhua@xust.edu.cn (Y.L.); l.zhang@ecu.edu.au (L.-C.Z.); Tel.: +86–029–8558–3159 (Y.L.)

Abstract: Although introducing high porosity in biomedical Ti alloys can reduce their elastic modulus and promote new bone ingrowth, relieving the stress–shielding effect and implant failure, this also causes a decline in the alloys' mechanical strength. In this work, a new preparation method for the high–strength and high–porosity $Ti_{65}Nb_{23.33}Zr_5Ta_{1.67}Fe_5$ (TNZTF, at.%) alloy was suggested by sintering nanocomposite powder precursor in combination with the use of a space holder technique, in which NH_4HCO_3 is adopted to achieve a porous structure. The highly porous TNZTF alloy possesses a homogeneous fine–grained microstructure consisting of equiaxed α–Ti and a small amount of $FeTi_2$, the latter of which is distributed in the β–Ti matrix. Through adjusting the mass fraction of NH_4HCO_3, a novel high–porosity, and high–strength TNZTF alloy with a low modulus was successfully prepared. The porous alloy with the addition of 30 wt.% NH_4HCO_3 exhibits a porosity of 50.3 ± 0.2%, a maximum strength of 327.3 ± 2.1 MPa, and an elastic modulus of 12.2 ± 0.3 GPa. The strength enhancement is mainly attributed to the unique fine–grained microstructure, which is obtained by the crystallization of the amorphous phase and the ductile–brittle mixed fracture mechanism. The prepared porous TNZTF alloy possesses higher mechanical strength and well–matched elastic modulus, showing great potential as an implant material.

Keywords: porous TiNbZrTaFe alloys; powder metallurgy; pore structure; microstructure; mechanical property

check for updates

Citation: Li, Y.; He, Y.; Zhao, R.; Niu, L.; Qu, J.; Zhang, L.-C. High–Strength Porous TiNbZrTaFe Alloys Fabricated by Sintering of Nanocomposite Powder Precursor with Space Holder Technique. *Metals* **2024**, *14*, 824. https://doi.org/10.3390/met14070824

Academic Editors: Eric Hug, Jose Manuel Torralba and Yongho Sohn

Received: 18 May 2024
Revised: 14 July 2024
Accepted: 15 July 2024
Published: 18 July 2024

Copyright: © 2024 by the authors. Licensee MDPI, Basel, Switzerland. This article is an open access article distributed under the terms and conditions of the Creative Commons Attribution (CC BY) license (https://creativecommons.org/licenses/by/4.0/).

1. Introduction

With the rapid growth of an aging population, the requirement for implant materials is increasing [1]. Metals, when applied as implant materials, display remarkable preponderances compared with polymers and ceramics, e.g., high strength and high plasticity [2,3]. Among the metallic implant materials, Ti and Ti alloys are widely applicable for orthopedic and dental implants due to their excellent properties, e.g., favorable biocompatibility, as well as good anti–wear and anti–corrosion ability [4–7]. In particular, β–Ti alloys that are composed of biocompatible elements, e.g., Ti, Nb, Zr, Hf, Mo, and Si, etc. [8], are gaining acceptance for biomedical devices, owing to their relatively low modulus and biocompatibility [9]. Representative examples of biomedical β–Ti alloys include TiZrNb [10], TiMoSi [11], TiNb [12], TiZrHfNbFe [13], TiNbZrMo [14], and TiZrNbTa [15]. However, one of the dominant problems regarding the recently developed β–Ti biomaterials is the elastic modulus mismatch of implants to bone. When the elastic modulus of implant materials is higher than the bone, it may cause a stress–shielding effect and implant failure [16,17]. Ti and Ti alloys that are designed for implantation must have high strength along with a low modulus that matches the human bone.

Porous metallic biomaterials have been developed to solve the aforementioned issue by reducing the elastic modulus of implant materials. Porous structures could effectively reduce the elastic modulus of biomaterials by regulating porosity parameters [18]. This can provide earlier mechanical stabilization to avoid premature mobility by improving the stress transfer between implant materials and bone [19]. It was proved that porous Ti–based biomaterials with high porosity can effectively promote bone regeneration and ingrowth [20]. A porosity level greater than 45% is required to acquire matched elastic modulus to the bones [21]. Increasing porosity reduces elastic modulus but this also declines strength below the requirement for bone replacement [21–23]. Therefore, the preparation of high–porosity and high–strength porous biomedical titanium alloys remains both an academic hotspot and a challenge within this field.

The fabrication methods commonly used to acquire porous metallic materials are selective laser melting [24,25], field–assisted sintering [26,27], and powder metallurgy [28,29]. Powder metallurgy is extensively adopted in the production of porous materials owing to its near–net shape and favorable controllability [22,30]. By combining with space holder technology, powder metallurgy could acquire a substantial porosity of 35–80% and a uniform pore distribution and become an economically advantageous and flexible method [3,22,25,29]. For this method, the common space holders include NH_4HCO_3 [31–33], NaCl [27,34], Mg [35,36], saccharose [37], and carbamide [38], which can be removed through decomposition or dissolution process [4,22]. Owing to moderate decomposition temperature, NH_4HCO_3 can be easily and completely removed, and it has become one of the widely used space holders [22]. Chávez–Vásconez et al. [39] produced porous titanium using 50 vol.% NH_4HCO_3 via powder metallurgy, i.e., pressing at 400 MPa and then sintering at 750 °C in argon atmosphere. Ehtemam–Haghighi et al. [40] fabricated TiMoFe foams using different additions of NH_4HCO_3. Luo et al. [36] prepared Ti foam with porosities of 35–65% using Mg space holder, cold pressing at 400 MPa, and sintering at 1150 °C holding for 4 h in high–purity Ar atmosphere, and the Ti foam possesses a yield strength of 22–126 MPa and an elastic modulus of 0.063–1.18 GPa. Xie et al. [41] used sodium chloride to prepare porous TiZrCuPdSn bulk metallic glass by sintering at 1100 °C and 1200 °C under vacuum. Xiang et al. [42] reported a new magnesium oxide used as a space holder in the preparation of porous TiZrNbTa/Ti composite. Nevertheless, the sintering process always causes undesirable grain coarsening owing to high sintering temperature and long holding time [43]. The obtained Ti and its alloys with high porosity still showed drawbacks such as coarse grain and low strength [3,22,25]. Considering the mechanical performance, Ti and Ti alloys with a fine–grained structure have acquired attention, which leads to a dramatic increase in strength compared with the coarse–grained counterparts [6,44].

In this work, a new preparation method for high–strength Ti alloys with large porosity, low modulus, and fine–grained structure was suggested by sintering nanocomposite powder precursor in combination with the space holder technique. NH_4HCO_3 was adopted to achieve a porous structure. Through adjusting the mass fraction of NH_4HCO_3, a novel high–porosity and high–strength $Ti_{65}Nb_{23.33}Zr_5Ta_{1.67}Fe_5$ (TNZTF, at.%, the same hereafter) alloy with low modulus was successfully prepared. The selection of the TiNbZrTa alloy system was owing to its excellent biocompatibility and low elastic modulus [7,15,20,42]. Fe was selected as a minor component for a relatively low cost. Moreover, the minor Fe addition can promote glass formation and grain refinement [13,40]. The pore structure, microstructure, and mechanical performance of the porous TNZTF alloy are thoroughly discussed in this study. The highly porous high–strength TNZTF alloy with low modulus possesses the potential application as implant material.

2. Experimental Methods

$Ti_{65}Nb_{23.33}Zr_5Ta_{1.67}Fe_5$ (TNZTF) nanocomposite powder precursor was synthesized by mechanical milling of high–purity elemental powder mixtures with a particle size below 48 μm. The detailed synthesis steps of the nanocomposite powder precursor can be referred to our previous work [45,46]. During the milling process, a minor amount of

powder was taken out every 5 h using an argon–filled ZKX2 glovebox (Nanjing Nanda Instrument Co., Ltd., Nanjing, China) for characterization. The as–milled powders were mixed with NH_4HCO_3 with a particle size of 325–425 μm in a V–5L mixer (Wuxi Cheng Ming Drying Equipment Co., Ltd., Wuxi, China) for 45 min at 100 rpm. The mixtures were cold pressed into a square shape with 500 MPa in a YAW4106 electro–hydraulic servo press (Sans Testing Machine Co., Ltd., Shanghai, China). The green compacts with dimensions of 15 × 15 × 10 mm were sintered in an FGL–70/17/2 vacuum atmosphere tube furnace (Hefei FACEROM Thermal Equipment Co., Ltd., Hefei, China) with high–purity argon atmosphere protection. The first step was performed at 80 °C for 2 h, then the green compacts were heated to 175 °C at 3 °C/min and held for 1 h to eliminate the NH_4HCO_3 and excess water, and then heated to 1200 °C at 5 °C/min and held for 3 h. The sintering temperature was far higher than the onset crystallization temperature T_x (~788 °C). This temperature was used to acquire crystallized bulk porous alloys by crystallization of the amorphous phase. The as–fabricated porous TNZTF samples with 30, 40, and 50 wt.% NH_4HCO_3 are hereafter referred to as S30, S40, and S50.

The thermal behavior of the as–milled powder was analyzed by STA449C differential scanning calorimetry (DSC; NETSCH, Hanau, Germany) in a high–purity Ar atmosphere at 20 °C/min. The phase constitution and microstructure of the as–milled powder were analyzed using D/MAX–2500/PC X–ray diffraction (XRD; Rigaku Corp., Tokyo, Japan) with Cu K_α radiation (λ = 1.5418 Å) and step size of 0.02°, Nova NanoSEM430 scanning electron microscope (SEM; FEI, Hillsboro, OR, USA) and Tecnai G2 F30 field emission transmission electron microscope (TEM; FEI, Eindhoven, The Netherlands). The phase constitution, microstructure, fracture morphology, and uniaxial compressive properties of the as–prepared porous samples were characterized through XRD, SEM, and an MTS Test Star 810 testing system (Oak Ridge, TN, USA). The detailed procedures can be found in the literature, e.g., Refs [45,46]. Pore features in terms of morphology, size, and roundness of the as–sintered porous samples were investigated by LEICA/DMI 5000M optical microscope (OM; Wetzlar, Germany) combined with quantitative analysis by Image J analyzer. The calculation and experimental procedures of the general porosity for the as–fabricated porous samples can be seen in Ref. [47].

3. Results and Discussion

3.1. Characterization of the as–Milled TNZTF Powder

Figure 1a shows the XRD result of 115 h–milled TNZTF powder. The diffraction peaks of β–Ti have a certain degree of broadening with relatively low intensity, indicating grain refinement or glass formation. DSC analysis (Figure 1b) suggests that the 115 h–milled powder exhibits a crystallization exothermic peak with a crystallization temperature (T_x) of about 788 °C, which indicates the formation of an amorphous phase during mechanical alloying. Furthermore, this demonstrates that the 115 h–milled powder undergoes crystallization of the amorphous phase including grain nucleation and growth during the subsequent sintering process. The 115 h–milled powder shows agglomeration of particles with an agglomerate size of about 25 μm, implying the existence of an amorphous phase, and with particle size below 25 μm (Figure 1c), which is much smaller than the size of the original elemental powders (about 48 μm). This is attributed to the violent collision, work hardening, and brittle fracture during mechanical milling. Further TEM analysis (Figure 1d) indicates that the 115 h–milled powder possesses a nanocomposite microstructure, which has a few β–Ti nanocrystallines distributed in the glassy matrix. This is in accordance with the XRD and DSC results.

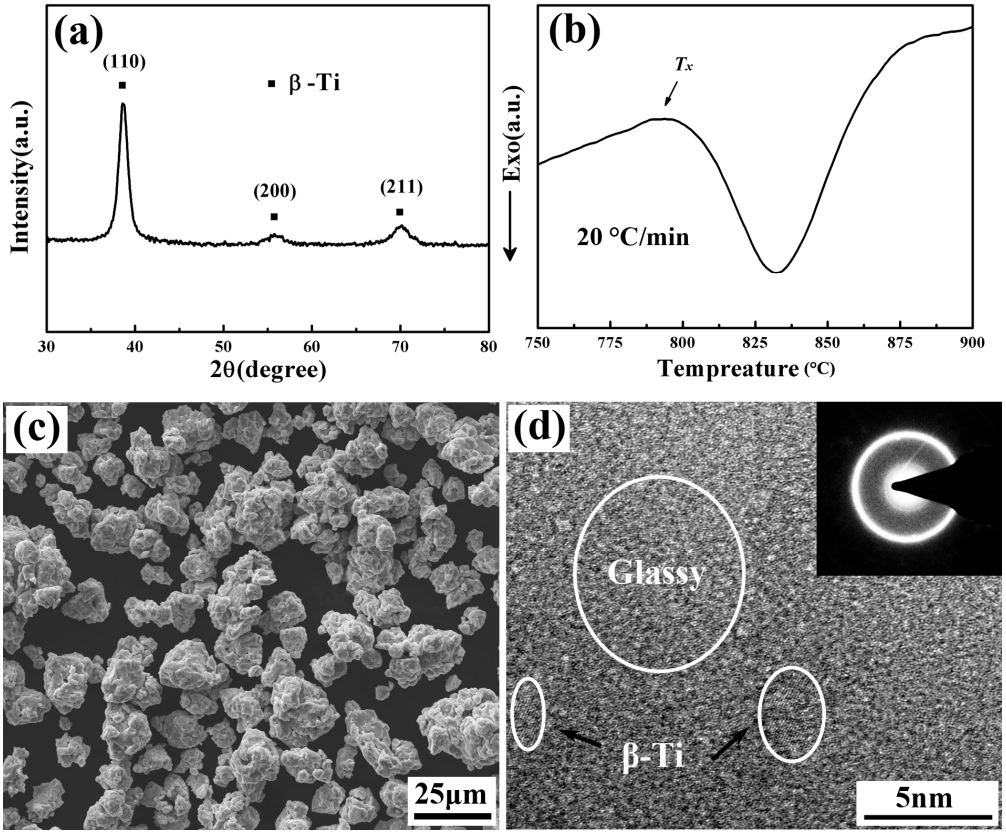

Figure 1. (**a**) XRD pattern, (**b**) DSC curve, (**c**) SEM morphology, and (**d**) TEM bright–field image and corresponding selected area diffraction (SAED) pattern of the 115 h–milled TNZTF powder.

3.2. Pore Structure Characterization of the as–Prepared Porous TNZTF Alloys

The pore structure characteristics of porous materials comprise three aspects, i.e., porosity, pore size, and pore shape. As shown in Figure 2, the porosity of the porous S30, S40, and S50 samples increases from 50.3% to 66.2% as the mass fraction of NH_4HCO_3 increases from 30% to 50%. Zhang et al. [48] reported that increasing porosity is very important for cell ingrowth and the benefits of producing an interconnected porous structure for body fluid transport. This indicates that the porosity obtained in the as–fabricated, porous alloys is favorable to new bone ingrowth.

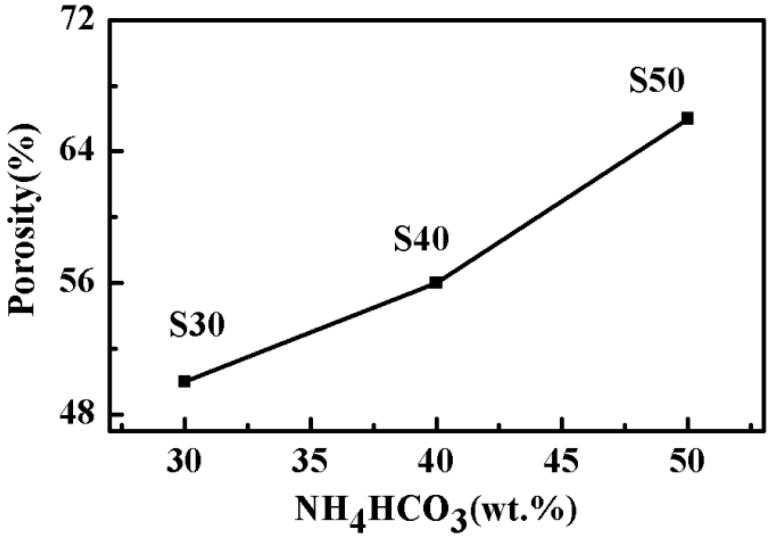

Figure 2. Effect of NH_4HCO_3 addition on the porosity of the as–fabricated porous TNZTF samples.

Figure 3 shows the pore morphologies of the porous S30, S40, and S50 samples. As seen from the figure, all the samples display a three–dimensional interconnected porous structure. The porous samples mainly include two types of pores; one is uniformly distributed and interconnected macropores (Figure 3a,c,e), which are formed by the elimination of NH_4HCO_3, and the other is isolated micropores (Figure 3a,c,e) distributed in the macropore walls, which are formed due to the incomplete sintering of the constituent powders. This is in accordance with the results reported in the literature, e.g., Refs [22,34,39]. The addition of high NH_4HCO_3 content can increase the levels of pore interconnectivity (Figure 3a,c,e). The interconnected macropores are conducive to the transportation of nutrients and the adhesion, differentiation, and growth of bone cells, providing sufficient space for the growth of new bone and therefore realizing the biological fixation of implants [48]. The micropores can promote the rapid growth of a new bone, and the mutual penetration of bone cells and nutrients, and accelerate bone integration [48]. The Image J software (Version number 1.42q) was used to process pore morphologies after binarization (Figure 3b,d,f). After analysis and statistics, pore characteristics such as pore size distribution (Figure 4) and pore roundness distribution (Figure 5) were obtained.

As shown in Figure 4a, the 400–500 μm pores account for about 30% and they contribute the most to the porosity in S30. The 100–200 μm, 200–300 μm, and 300–400 μm pores occupy about the same proportion and therefore they almost equally contribute to the porosity. The 400–500 μm and 500–600 μm pores account for 65% of S40 (Figure 4b), among which the pores of 500–600 μm take about 40%. The 600–700 μm pores contribute the most to the porosity of S50 (Figure 4c), accounting for about 43%. This indicates that the pore size increases as the NH_4HCO_3 content increases from 30% to 50%. The pores above 200 μm in size are the main part of all the porous samples (Figure 4a–c), which is conducive to new bone tissue ingrowth. For S30 (Figure 4d), pore roundness decreases with the increase in pore size. The roundness for pores above 150 μm in size is below 0.4. This suggests that the larger the pore, the less the pore roundness.

As shown in Figure 5, the pore roundness of the porous S30, S40, and S50 samples mainly ranges from 0 to 0.1. As shown in Figure 5a, the percentage of roundness range of 0–0.1, 0.1–0.2, and 0.2–0.3 in the S30 samples is about 48%, 30%, and 9%, respectively. The average roundness is about 0.15. As shown in Figure 5b, the percentage of roundness range of 0–0.1, 0.1–0.2, and 0.2–0.3 in the S40 is about 58%, 28%, and 5%, respectively, and the average roundness is about 0.10. As shown in Figure 5c, the roundness of S50 mainly ranges from 0 to 0.1, accounting for about 73%, and the average roundness is about 0.05. This suggests that the pores of S30, S40, and S50 are mainly elliptical, which is consistent with the pore morphologies shown in Figure 3. As increasing the NH_4HCO_3 content from 30% to 50%, the roundness of the porous samples decreases to a certain extent. As shown in Figure 5d, the roundness of S50 decreases as the pore size increases. The roundness of pores above 100 μm in size is below 0.4. This indicates that the greater the pore size, the more irregular the pore shape. This is in accordance with the results of S30 (Figure 4d). This suggests that with the increase in NH_4HCO_3 addition, both the porosity (Figure 2) and pore size (Figure 4) increase, while the pore roundness (Figure 5) decreases for the as–fabricated porous alloys, as proved through the pore morphologies shown in Figure 3.

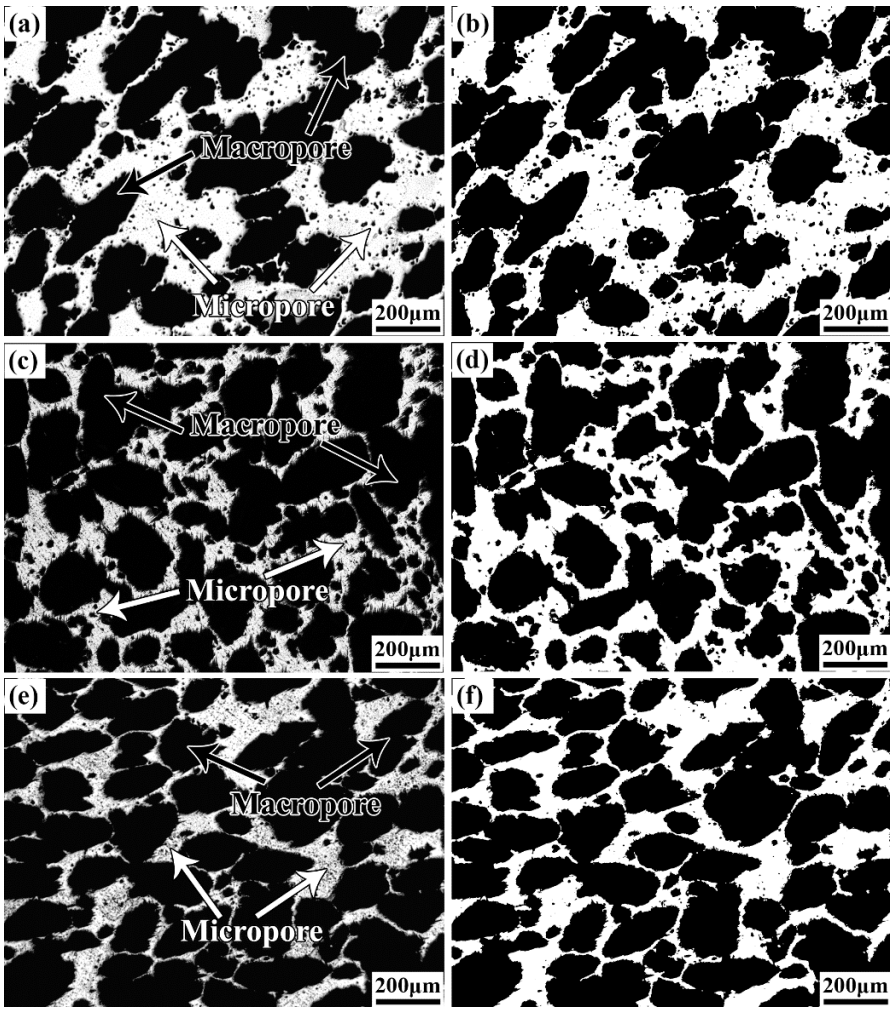

Figure 3. Pore morphologies of the as–fabricated porous TNZTF samples and the corresponding pore images after binarization: (**a**,**b**) S30, (**c**,**d**) S40, and (**e**,**f**) S50.

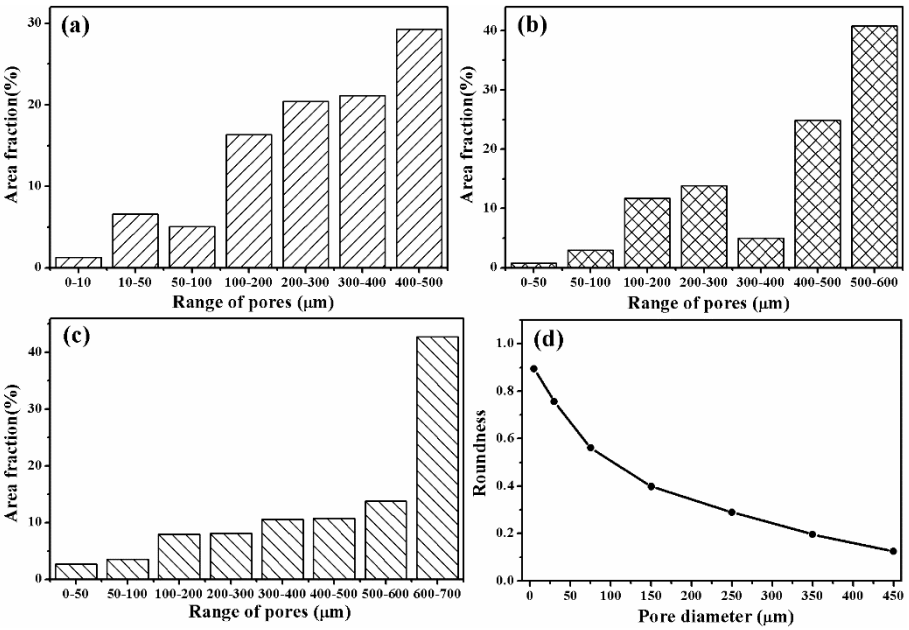

Figure 4. Pore size distribution of the as–fabricated porous TNZTF samples: (**a**) S30, (**b**) S40, and (**c**) S50; (**d**) relationship between roundness and pore diameter for S30.

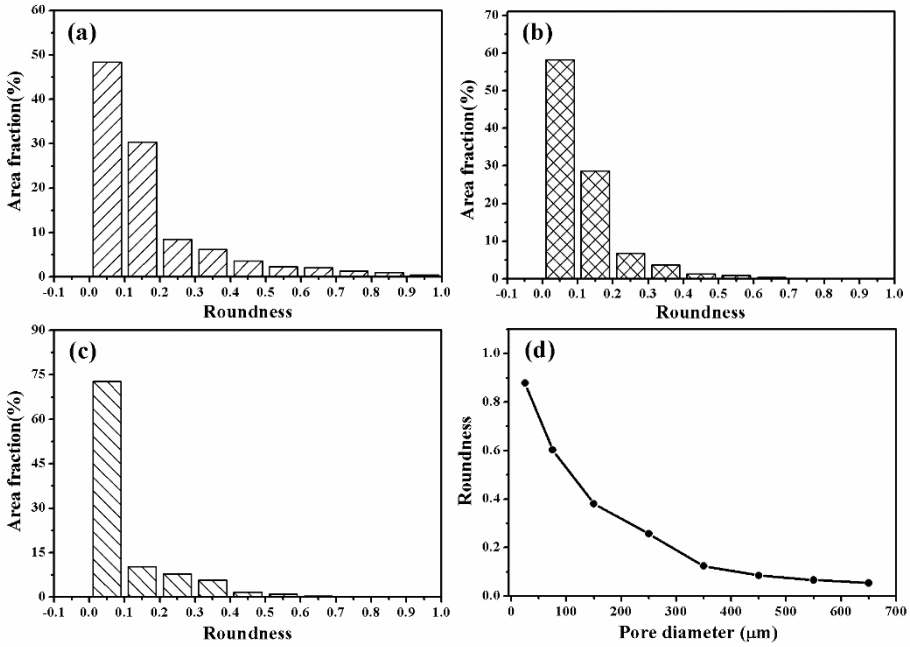

Figure 5. Pore roundness distribution of the as–fabricated porous TNZTF samples: (**a**) S30, (**b**) S40, and (**c**) S50; (**d**) relationship between roundness and pore diameter for S50.

3.3. Phase Constitution and Microstructure of the as–Fabricated, Porous TNZTF Alloys

Figure 6 shows XRD patterns and SEM microstructures of the as–fabricated porous TNZTF samples. According to the XRD results, there are no diffraction peaks for elemental powders, and the porous S30, S40, and S50 samples are mainly composed of β–Ti with minor α–Ti and $FeTi_2$, indicating the complete alloying of constituent elements. The phase constitutions have little change upon the addition of NH_4HCO_3 increasing from 30 to 50%. It is well known that Nb, Ta, and Fe are the β–Ti stabilizers, and the Ti–Zr system exhibits a complete substitutional solid solution. By crystallization of the glassy phase, the as–milled pre–alloyed nanocomposite powder precursor with different NH_4HCO_3 additions was sintered under identical sintering parameters, thereby demonstrating little effect on the phase constitutions of the crystallized phases.

According to the SEM results (Figure 6), the porous S30, S40, and S50 samples possess a relatively homogeneous microstructure composed of equiaxed α–Ti and a small amount of $FeTi_2$ distributed in the β–Ti matrix compared with the results in Ref. [47]. The α–Ti phase in S50 tends to spheroidize. The average grain size of β–Ti in the porous S30, S40, and S50 samples was about 4.96 ± 0.32, 5.08 ± 0.43, and 5.05 ± 0.41 μm, respectively, while the value for α–Ti was about 1.87 ± 0.02, 2.15 ± 0.03, and 2.03 ± 0.02 μm, respectively, and the value for $FeTi_2$ was about 0.70 ± 0.05, 0.77 ± 0.06, and 0.76 ± 0.06 μm, respectively. Furthermore, the average sizes of the β–Ti, α–Ti, and $FeTi_2$ firstly increase and then decrease slightly as the addition of NH_4HCO_3 increases from 30% to 50%, which is in accordance with the XRD results. This trend is more evident for α–Ti. During the consolidation and crystallization of the nanocomposite powder precursor, powder metallurgy bonding is firstly dominated by viscous flow and then atom diffusion [49]. The diffusion between powder particles is hindered to a certain extent due to the increasing porosity and pore size, and thus the crystallized precipitates inside the particles tend to grow during the crystallization process. When the porosity increases to 66%, the viscous flow is probably confined and may lead to hysteretic crystallization behavior, which is beneficial to inhibiting the growth of the crystallized phase [50,51]. This will be further investigated in a future study. The micropores formed due to the incomplete sintering of the constituent powders are observed clearly from the S50 sample (Figure 6). According to the classical nucleation and growth theory, grain boundary migration and grain growth may also be restricted due to the micropores formed during the sintering process. Compared with the porous

TiNbZrFe alloy prepared from elemental blended powders in our previous work [47], the phase distribution of the porous S30, S40, and S50 samples prepared from the pre–alloyed nanocomposite powder precursor is remarkably more homogeneous. Furthermore, the porous S30, S40, and S50 samples have very fine grains, which is in accordance with the results reported by Awad et al. [52]. This highlights the advantages of through sintering of nanocomposite powder precursor in combination with the space holder technique in preparing fine–grained porous titanium alloys for biomedical applications.

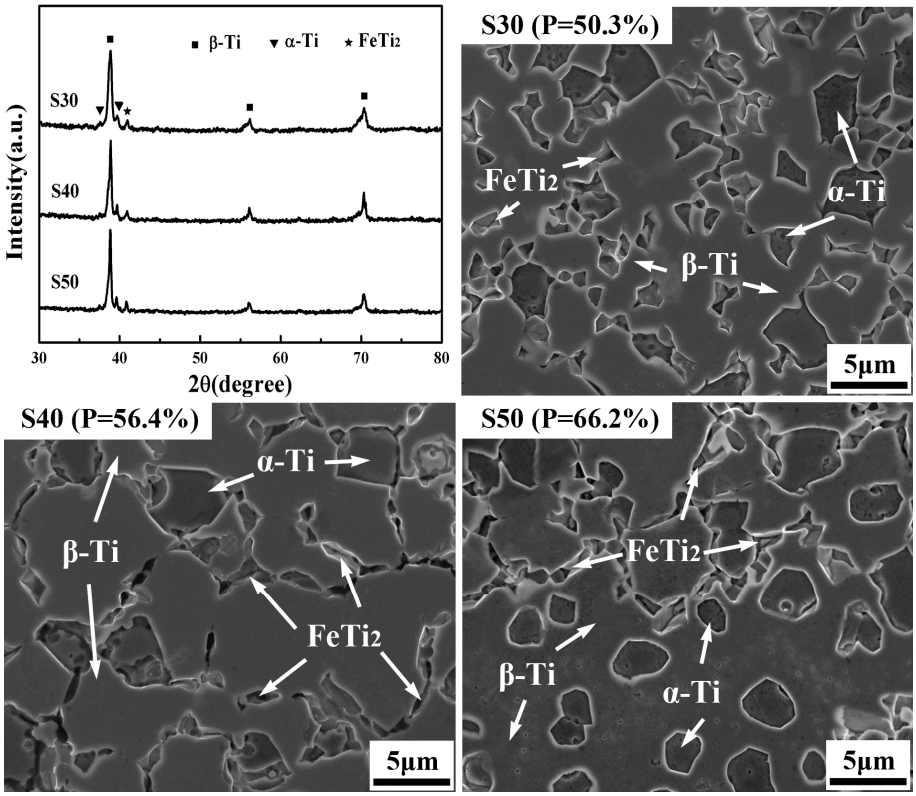

Figure 6. XRD patterns and SEM microstructures of the as–fabricated porous TNZTF samples.

3.4. Mechanical Property of the as–Prepared TNZTF Porous Alloys

Due to the introduction of pores, the mechanical performance of porous materials is inevitably reduced compared with dense materials with the same composition, and their deformation behavior is also different [36,39]. The mechanical performance of porous titanium alloys is usually determined by pore characteristics and microstructure [3,22]. The microstructure could generate an enormous effect on yield strength and plasticity. The influence of pore characteristics on the strength of porous materials is mainly manifested as follows [34,36]. Firstly, the existence of pores reduces the actual cross–sectional area and strength. Secondly, stress concentration occurs easily near the pores, which affects the fracture toughness. The degree of stress concentration is related to the pore size and pore shape. Thirdly, pores provide space for deformation and affect the fracture behavior of porous materials. The increase in porosity and pore irregularity and the decrease in pore curvature radius may cause stress concentration therefore the strength reduction. By contrast, pore spheroidization can reduce stress concentration. Figure 7 shows the compressive engineering stress–strain curves of the porous S30, S40, and S50 samples. As deduced from the curves, the strength decreases as increasing the NH_4HCO_3 addition. As stress reaches maximum, brittle failure does not occur immediately, yet deformation continues under low stress brought about by the porous structure, indicating that the porous samples have a certain plasticity, which is conducive to implants for biomedical applications. Meanwhile, from the stress–strain curves, two distinct regions are observed during deformation; one is a linear elastic region, and the other is a plateau stage with stress

fluctuation. This is probably attributed to the increase in pore irregularity as increasing the NH_4HCO_3 addition, which results in stress concentration and strain localization [36]. In this work, no densification stage is noted in the limited strain. The deformation is characterized by elastic buckling, bending, and collapse of cell walls for the porous samples [36,39]. Additionally, compared with the porous TiNbZrFe alloy prepared from elemental blended powders [47], the porous TNZTF samples prepared from the pre–alloyed nanocomposite powder precursor exhibit much higher compressive strength (Table 1). This is mainly attributed to the homogeneous equiaxed and fine–grained microstructure obtained.

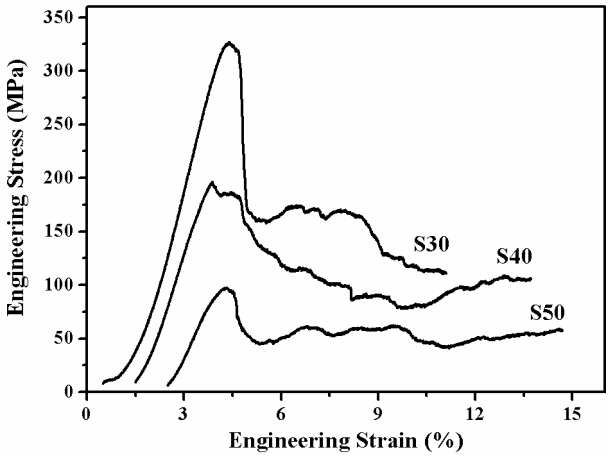

Figure 7. Compressive stress–strain curves of the as–fabricated porous TNZTF samples.

Table 1. Summary of the mechanical properties of the as–fabricated porous TNZTF samples.

Samples	NH_4HCO_3 (wt.%)	Porosity (%)	Elastic Modulus (GPa)	Compressive Strength (MPa)
S30	30	50.3 ± 0.2	12.2 ± 0.3	327.3 ± 2.1
S40	40	56.4 ± 0.4	9.7 ± 0.2	197.2 ± 1.2
S50	50	66.2 ± 0.6	6.4 ± 0.1	98.4 ± 0.6
$Ti_{59.38}Nb_{26.6}Zr_{8.7}Fe_{5.32}$ [47]	30	48	11	165
$Ti_{59.38}Nb_{26.6}Zr_{8.7}Fe_{5.32}$ [47]	40	53	7	117

As shown in Table 1, as the mass fraction of NH_4HCO_3 increases from 30% to 50%, the elastic modulus and compressive strength of the porous samples decreases from 12.2 GPa to 6.4 GPa and from 327.3 MPa to 98.4 MPa, respectively. This can well satisfy the mechanical property requirements of the human cortical bone with a compressive strength of 20–193 MPa and elastic modulus of 4–30 GPa [3]. The elastic modulus could be modulated to match that of bone by changing the NH_4HCO_3 addition.

As shown in Figure 7 and Table 1, the porous TNZTF sample with 30 wt.% NH_4HCO_3 possesses higher strength than other porous materials, e.g., porous Ti, Ti–10Mo foams, and porous TiZrNbTa/Ti composite, TiNbZrFe foams, etc. [36,42,43,47]. Compared to dense materials, e.g., Ti and Ti alloys, CoCr alloys, and 316 L stainless steel [2,3], the porous TNZTF samples show a distinct advantage in terms of elastic modulus modulation. Considering high strength, low elastic modulus, high porosity, and non–toxic constituent elements, the as–fabricated porous TNZTF samples have great potential for clinical application.

Figure 8 displays the SEM fracture morphologies of the porous samples. From the low–magnification fracture morphologies (Figure 8a,c,e), macropores and micropores can be observed clearly. The porous S50 sample with 50 wt.% NH_4HCO_3 addition exhibits pore collapse (Figure 8e). For the pore walls, the deformation begins from weaker and thinner areas until failure and collapse which eventually occurs as the stress increases, which is in accordance with the results shown in Figure 7. From the high–magnification fracture morphologies, the micropores can be seen clearly (Figure 8b,d,f), which is in alignment

with the results shown in Figure 6. The fracture mode of the as–fabricated porous TNZTF samples indicates ductile–brittle mixed fracture characteristics. The α–Ti phase regions display a rock candy structure showing brittle breakage characteristics, while the β–Ti phase regions display a pull–out dimple structure indicating ductile fracture characteristics. The cracks are mainly generated from the α–Ti phase regions indicating the typical trans–granular fracture characteristics. This is mainly because the β–Ti matrix has better plastic deformation ability than the α–Ti phase.

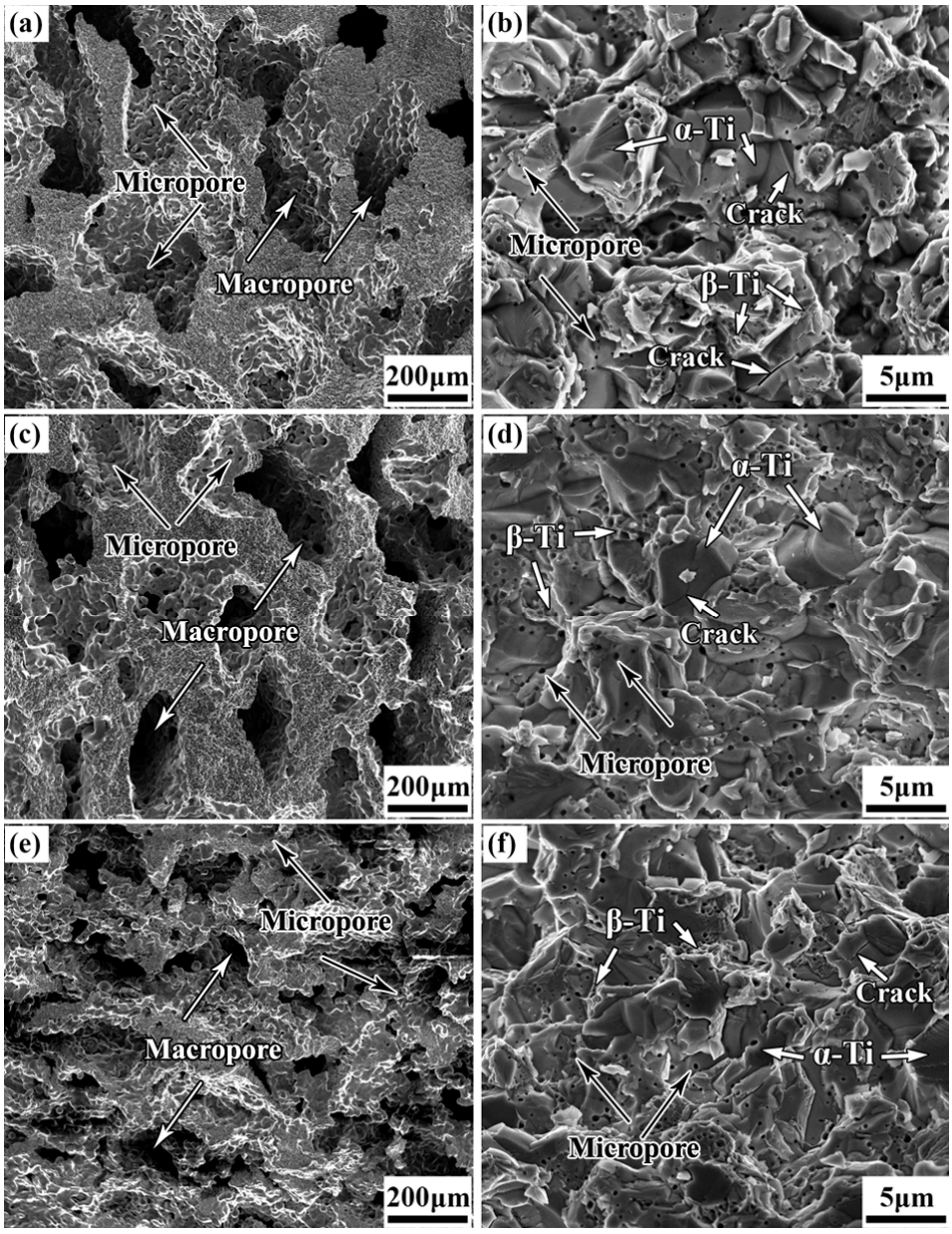

Figure 8. SEM fracture morphologies at low and high magnification of the as–fabricated porous TNZTF samples: (**a**,**b**) S30, (**c**,**d**) S40, and (**e**,**f**) S50.

4. Conclusions

In this work, the highly porous high–strength TiNbZrTaFe alloys were successfully prepared by a new preparation method through the sintering of nanocomposite powder precursor in combination with NH_4HCO_3 as a space holder. They demonstrate a porosity of 50.3–66.2%, an elastic modulus of 6.4–12.2 GPa, and a compressive strength

of 98.4–327.3 MPa. According to the systematic investigation of the pore characteristics, microstructure, and mechanical performance, the conclusions can be obtained as follows:

1. The porous samples possess a homogeneous and fine–grained microstructure composed of equiaxed α–Ti and a small amount of $FeTi_2$ dispersed in the β–Ti matrix. While being capable of adjusting pore structure characteristics and mechanical properties by a large margin, the addition of NH_4HCO_3 from 30 to 50 wt.% has little effect on their phase constitutions. The average grain size first increases and then decreases slightly with the increase in NH_4HCO_3 addition. The fracture mechanism indicates ductile–brittle mixed fracture characteristics in which β–Ti phase regions show a dimple structure while α–Ti phase regions display a rock candy structure together with trans–granular cracks.
2. The porous alloy with a porosity of 50.3 ± 0.2% shows an excellent combination of mechanical properties with a compressive strength of 327.3 ± 2.1 MPa, and an elastic modulus of 12.2 ± 0.3 GPa, respectively. Compared with other porous titanium biomaterials, it exhibits a higher compressive strength and a low elastic modulus matched to that of the human bones. The strength enhancement is mainly attributed to the unique fine–grained microstructure obtained by the crystallization of the amorphous phase during sintering and the ductile–brittle mixed fracture mechanism.

Author Contributions: Conceptualization, Y.L. and L.N.; methodology, Y.L. and J.Q.; software, Y.H. and R.Z.; validation, Y.H. and R.Z.; formal analysis, Y.L. and J.Q.; investigation, Y.L.; resources, Y.L. and L.N.; data curation, Y.L.; writing—original draft preparation, Y.L.; writing—review and editing, Y.H., J.Q., and L.-C.Z.; visualization, Y.H. and R.Z.; supervision, L.-C.Z.; project administration, Y.L.; funding acquisition, Y.L. and L.N. All authors have read and agreed to the published version of the manuscript.

Funding: This research was funded by the China Postdoctoral Science Foundation (Grant No. 2018M643690), the Natural Science Basic Research Plan in Shaanxi Province of China (Grant No. 2018JQ5087), the Open Funds of National Engineering Research Center of Near–Net–Shape Forming for Metallic Materials (Grant No. 2008002), and the Key Research and Development Program of Shaanxi Province (Grant No. 2023–YBGY–090).

Data Availability Statement: The original contributions presented in the study are included in the article, further inquiries can be directed to the corresponding authors.

Conflicts of Interest: The authors declare no conflicts of interest.

References

1. Sebbag, E.; Felten, R.; Sagez, F.; Sibilia, J.; Devilliers, H.; Arnaud, L. The world–wide burden of musculoskeletal diseases: A systematic analysis of the world health organization burden of diseases database. *Ann. Rheum. Dis.* **2019**, *78*, 844–848. [CrossRef] [PubMed]
2. Cui, Y.W.; Wang, L.Q.; Zhang, L.C. Towards load–bearing biomedical titanium–based alloys: From essential requirements to future developments. *Prog. Mater. Sci.* **2024**, *144*, 101277. [CrossRef]
3. Li, Y.H.; Yang, C.; Zhao, H.D.; Qu, S.G.; Li, X.Q.; Li, Y.Y. New developments of Ti–based alloys for biomedical applications. *Materials* **2014**, *7*, 1709–1800. [CrossRef] [PubMed]
4. Pitchi, C.S.; Priyadarshini, A.; Sana, G.; Narala, S.K.R. A review on alloy composition and synthesis of β–Titanium alloys for biomedical applications. *Mater. Today Proc.* **2020**, *26*, 3297–3304. [CrossRef]
5. Ma, H.Y.; Wang, J.C.; Qin, P.; Liu, Y.J.; Chen, L.Y.; Wang, L.Q.; Zhang, L.C. Advances in additively manufactured titanium alloys by powder bed fusion and directed energy deposition: Microstructure, defects, and mechanical behavior. *J. Mater. Sci. Technol.* **2024**, *183*, 32–62. [CrossRef]
6. Li, Y.H.; Zhang, Q.; He, Y.X.; Zhao, R.; Chu, J.H.; Niu, L.B.; Qu, J.X. Sliding and fretting wear behavior of biomedical ultrafine–grained TiNbZrTaFe/Si alloys in simulated physiological solution. *Materials* **2024**, *17*, 787. [CrossRef] [PubMed]
7. Li, B.Q.; Xie, R.Z.; Lu, X. Microstructure, mechanical property and corrosion behavior of porous Ti–Ta–Nb–Zr. *Bioact. Mater.* **2020**, *5*, 564–568. [CrossRef] [PubMed]
8. Song, C.H.; Liu, L.S.; Deng, Z.T.; Lei, H.Y.; Yuan, F.Z.; Yang, Y.Q.; Li, Y.Y.; Yu, J.K. Research progress on the design and performance of porous titanium alloy bone implants. *J. Mater. Res. Technol.* **2023**, *23*, 2626–2641. [CrossRef]
9. Zhang, L.C.; Chen, L.Y.; Zhou, S.F.; Luo, Z. Powder bed fusion manufacturing of beta–type titanium alloys for biomedical implant applications: A review. *J. Alloys Compd.* **2023**, *936*, 168099. [CrossRef]

10. Xu, W.; Lu, X.; Tian, J.J.; Huang, C.; Chen, M.; Yan, Y.; Wang, L.N.; Qu, X.H.; Wen, C. Microstructure, wear resistance, and corrosion performance of Ti35Zr28Nb alloy fabricated by powder metallurgy for orthopedic applications. *J. Mater. Sci. Technol.* **2020**, *41*, 191–198. [CrossRef]
11. El–Sayed Seleman, M.M.; Ataya, S.; Aly, H.A.; Haldar, B.; Alsaleh, N.A.; Ahmed, M.M.Z.; Bakkar, A.; Ibrahim, K.M. Effect of the Si content on the dry and wet sliding wear behavior of the developed Ti–15Mo–(0–2) Si alloys for biomedical applications. *Metals* **2023**, *13*, 1861. [CrossRef]
12. Wang, J.C.; Liu, Y.J.; Rabadia, C.D.; Liang, S.X.; Sercombe, T.B.; Zhang, L.C. Microstructural homogeneity and mechanical behavior of a selective laser melted Ti–35Nb alloy produced from an elemental powder mixture. *J. Mater. Sci. Technol.* **2021**, *61*, 221–233. [CrossRef]
13. Wang, W.J.; Yang, K.H.; Wang, Q.T.; Dai, P.Q.; Fang, H.; Wu, F.J.; Guo, Q.H.; Liaw, P.K.; Hua, N.B. Novel Ti–Zr–Hf–Nb–Fe refractory high–entropy alloys for potential biomedical applications. *J. Alloys Compd.* **2022**, *906*, 164383. [CrossRef]
14. Tong, X.; Sun, Q.X.; Zhang, D.C.; Wang, K.; Dai, Y.L.; Shi, Z.M.; Li, Y.C.; Dargusch, M.; Huang, S.B.; Ma, J.F.; et al. Impact of scandium on mechanical properties, corrosion behavior, friction and wear performance, and cytotoxicity of a β–type Ti–24Nb–38Zr–2Mo alloy for orthopedic applications. *Acta Biomater.* **2021**, *134*, 791–803. [CrossRef] [PubMed]
15. Xiang, T.; Du, P.; Cai, Z.Y.; Li, K.; Bao, W.Z.; Yang, X.X.; Xie, G.Q. Phase–tunable equiatomic and non–equiatomic Ti–Zr–Nb–Ta high–entropy alloys with ultrahigh strength for metallic biomaterials. *J. Mater. Sci. Technol.* **2022**, *117*, 196–206. [CrossRef]
16. Lee, T.; Lee, S.; Kim, I.S.; Moon, Y.H.; Kim, H.S.; Park, C.H. Breaking the limit of Young's modulus in low–cost Ti–Nb–Zr alloy for biomedical implant applications. *J. Alloys Compd.* **2020**, *828*, 154401. [CrossRef]
17. Yilmaz, E.; Gökçe, A.; Findik, F.; Gulsoy, H. Metallurgical properties and biomimetic HA deposition performance of Ti–Nb PIM alloys. *J. Alloys Compd.* **2018**, *746*, 301–313. [CrossRef]
18. Li, F.P.; Jia, T.; Dang, W.; Xu, Z.L.; Zhao, K.; Tang, Y.F. Porous Ti6Al4V alloys with high strength–to–modulus ratio fabricated by unidirectional freeze casting of SiC fiber–containing slurry. *Mater. Sci. Eng. A* **2021**, *820*, 141584. [CrossRef]
19. Wang, S.; Liu, L.; Li, K.; Zhu, L.; Chen, J.; Hao, Y. Pore functionally graded Ti6Al4V scaffolds for bone tissue engineering application. *Mater. Des.* **2019**, *168*, 107643. [CrossRef]
20. Hafeez, N.; Liu, J.; Wang, L.Q.; Wei, D.X.; Tang, Y.J.; Lu, W.J.; Zhang, L.C. Superelastic response of low–modulus porous beta–type Ti–35Nb–2Ta–3Zr alloy fabricated by laser powder bed fusion. *Addit. Manuf.* **2020**, *34*, 101264. [CrossRef]
21. Lascano, S.; Arévalo, C.; Montealegre–Melendez, I.; Muñoz, S.; Rodriguez–Ortiz, J.A.; Trueba, P.; Torres, Y. Porous Titanium for biomedical applications: Evaluation of the conventional powder metallurgy frontier and space–holder technique. *Appl. Sci.* **2019**, *9*, 982. [CrossRef]
22. Rodriguez–Contreras, A.; Punset, M.; Calero, J.A.; Gil, F.J.; Ruperez, E.; Manero, J.M. Powder metallurgy with space holder for porous titanium implants: A review. *J. Mater. Sci. Technol.* **2021**, *76*, 129–149. [CrossRef]
23. Abbasi, N.; Hamlet, S.; Love, R.M.; Nguyen, N.T. Porous scaffolds for bone regeneration. *J. Sci. Adv. Mater. Devices* **2020**, *5*, 1–9. [CrossRef]
24. Attar, H.; Ehtemam–Haghighi, S.; Soro, N.; Kent, D.; Dargusch, M.S. Additive manufacturing of low–cost porous titanium–based composites for biomedical applications: Advantages, challenges and opinion for future development. *J. Alloys Compd.* **2020**, *827*, 154263. [CrossRef]
25. Yang, X.L.; Du, X.F.; Xu, Z.L.; Liang, Z.S.; Xiong, L.L. Progress in processing of porous titanium: A review. *Rare Met.* **2024**, *43*, 1932–1955. [CrossRef]
26. Dudina, D.V.; Bokhonov, B.B.; Olevsky, E.A. Fabrication of porous materials by spark plasma sintering: A review. *Materials* **2019**, *12*, 541. [CrossRef]
27. Fujii, T.; Murakami, R.; Kobayashi, N.; Tohgo, K.; Shimamura, Y. Uniform porous and functionally graded porous titanium fabricated via space holder technique with spark plasma sintering for biomedical applications. *Adv. Powder Technol.* **2022**, *33*, 103598. [CrossRef]
28. Sauceda, S.; Lascano, S.; Béjar, L.; Neves, G.O.; Chicardi, E.; Salvo, C.; Aguilar, C. Study of the effect of the floating die compaction on mechanical properties of titanium foams. *Metals* **2020**, *10*, 1621. [CrossRef]
29. Yamanoglu, R.; Bahador, A.; Kondoh, K. Fabrication methods of porous titanium implants by powder metallurgy. *Trans. Indian Inst. Met.* **2021**, *74*, 2555–2567. [CrossRef]
30. Kumar, R.M.; Golla, B.R. Effect of space holder on porosity, structure and mechanical properties of Al processed via power metallurgy. *Trans. Indian Inst. Met.* **2021**, *74*, 2379–2386. [CrossRef]
31. Lascano, S.; Chávez–Vásconez, R.; Muñoz–Rojas, D.; Aristizabal, J.; Arce, B.; Parra, C.; Acevedo, C.; Orellana, N.; Reyes–Valenzuela, M.; Gotor, F.J.; et al. Graphene–coated Ti–Nb–Ta–Mn foams: A promising approach towards a suitable biomaterial for bone replacement. *Suf. Coat. Technol.* **2020**, *401*, 126250. [CrossRef]
32. Civantos, A.; Giner, M.; Trueba, P.; Lascano, S.; Montoya–García, M.J.; Arévalo, C.; Vázquez, M.A.; Allain, J.P.; Torres, Y. In vitro bone cell behavior on porous titanium samples: Influence of porosity by loose sintering and space holder techniques. *Metals* **2020**, *10*, 696. [CrossRef]
33. Gupta, J.; Ghosh, S.; Aravindan, S. Effect of Mo and space holder content on microstructure, mechanical and corrosion properties in Ti6AlxMo based alloy for bone implant. *Mater. Sci. Eng. C* **2021**, *123*, 111962. [CrossRef]
34. Lantang, Y.S.F.; Kobayashi, E.; Sato, T. Fabrication of spark plasma sintered porous Ti–6Al–4V using PCA–added space holder method for bone implant materials. *Mater. Today Proc.* **2022**, *66*, 2693–2701. [CrossRef]

35. Lai, T.; Xu, J.L.; Xiao, Q.F.; Tong, Y.X.; Huang, J.; Zhang, J.P.; Luo, J.M.; Liu, Y. Preparation and characterization of porous NiTi alloys synthesized by microwave sintering using Mg space holder. *Trans. Nonferrous Met. Soc. China* **2021**, *31*, 485–498. [CrossRef]
36. Luo, H.J.; Zhao, J.H.; Du, H.; Yin, W.; Qu, Y. Effect of Mg powder's particle size on structure and mechanical properties of Ti foam synthesized by space holder technique. *Materials* **2022**, *15*, 8863. [CrossRef] [PubMed]
37. Chen, Y.H.; Frith, J.E.; Dehghan–Manshadi, A.; Kent, D.; Bermingham, M.; Dargusch, M. Biocompatible porous titanium scaffolds produced using a novel space holder technique. *J. Biomed. Mater. Res. Part B Appl. Biomater.* **2018**, *106*, 2796–2806. [CrossRef] [PubMed]
38. Arifvianto, B.; Leeflang, M.A.; Zhou, J. The compression behaviors of titanium/carbamide powder mixtures in the preparation of biomedical titanium scaffolds with the space holder method. *Powder Technol.* **2015**, *284*, 112–121. [CrossRef]
39. Chávez–Vásconez, R.; Lascano, S.; Sauceda, S.; Reyes–Valenzuela, M.; Salvo, C.; Mangalaraja, R.V.; Gotor, F.J.; Arévalo, C.; Torres, Y. Effect of the processing parameters on the porosity and mechanical behavior of titanium samples with bimodal microstructure produced via hot pressing. *Materials* **2022**, *15*, 136. [CrossRef]
40. Ehtemam–Haghighi, S.; Attar, H.; Okulov, I.V.; Dargusch, M.S.; Kent, D. Microstructural evolution and mechanical properties of bulk and porous low–cost Ti–Mo–Fe alloys produced by powder metallurgy. *J. Alloys Compd.* **2021**, *853*, 156768. [CrossRef]
41. Xie, G.Q.; Kanetaka, H.; Kato, H.; Qin, F.X.; Wang, W. Porous Ti–based bulk metallic glass with excellent mechanical properties and good biocompatibility. *Intermetallics* **2019**, *105*, 153–162. [CrossRef]
42. Xiang, T.; Chen, J.; Bao, W.Z.; Zhong, S.Y.; Du, P.; Xie, G.Q. Fabrication of porous TiZrNbTa high–entropy alloys/Ti composite with high strength and low Young's modulus using a novel MgO space holder. *J. Mater. Sci. Technol.* **2023**, *167*, 56–73. [CrossRef]
43. Xu, W.; Liu, Z.; Lu, X.; Tian, J.J.; Chen, G.; Liu, B.W.; Li, Z.; Qu, X.H.; Wen, C. Porous Ti–10Mo alloy fabricated by powder metallurgy for promoting bone regeneration. *Sci. China Mater.* **2019**, *62*, 1053–1064. [CrossRef]
44. Zhang, J.Q.; Bermingham, M.J.; Otte, J.; Liu, Y.G.; Hou, Z.Y.; Yang, N.; Yin, Y.; Bayat, M.; Lin, W.K.; Huang, X.X.; et al. Ultrauniform, strong, and ductile 3D–printed titanium alloy through bifunctional alloy design. *Science* **2024**, *383*, 639–645. [CrossRef] [PubMed]
45. Li, Y.H.; Yang, C.; Wang, F.; Zhao, H.D.; Qu, S.G.; Li, X.Q.; Zhang, W.W.; Li, Y.Y. Biomedical TiNbZrTaSi alloys designed by *d*–electron alloy design theory. *Mater. Design* **2015**, *85*, 7–13. [CrossRef]
46. Li, Y.H.; Yang, C.; Kang, L.M.; Zhao, H.D.; Qu, S.G.; Li, X.Q.; Zhang, W.W.; Li, Y.Y. Non–isothermal and isothermal crystallization kinetics and their effect on microstructure of sintered and crystallized TiNbZrTaSi bulk alloys. *J. Non–Cryst. Solids* **2016**, *432*, 440–452. [CrossRef]
47. Li, Y.H.; Yang, C.; Kang, L.M.; Zhao, H.D.; Zhang, W.W.; Li, Y.Y. Biomedical porous TiNbZrFe alloys fabricated by using NH_4HCO_3 as pore–forming agent through powder metallurgy route. *Powder Metall.* **2015**, *58*, 228–234. [CrossRef]
48. Zhang, Y.N.; Sun, N.; Zhu, M.R.; Qiu, Q.R.; Zhao, P.J.; Zheng, C.Y.; Bai, Q.; Zeng, Q.Y.; Lu, T.L. The contribution of pore size and porosity of 3D printed porous titanium scaffolds to osteogenesis. *Biomater. Adv.* **2022**, *133*, 112651. [CrossRef] [PubMed]
49. Kamyabi, M.; Sotudeh–Gharebagh, R.; Zarghami, R.; Saleh, K. Principles of viscous sintering in amorphous powders: A critical review. *Chem. Eng. Res. Des.* **2017**, *125*, 328–347. [CrossRef]
50. Paul, T.; Harimkar, S.P. Viscous flow activation energy adaptation by isochronal spark plasma sintering. *Scr. Mater.* **2017**, *126*, 37–40. [CrossRef]
51. Cai, W.S.; Lu, H.Z.; Li, H.Z.; Liu, Z.; Ke, H.B.; Wang, W.H.; Yang, C. Microstructural evolution and superelastic properties of ultrafine–grained NiTi–based shape memory alloy via sintering of amorphous ribbon precursor. *J. Mater. Sci. Technol.* **2023**, *138*, 80–92. [CrossRef]
52. Awad, A.H.; Aly, H.A.; Saood, M. Physical, mechanical, and corrosion properties of Ti–12Mo and Ti–15Mo alloys fabricated by elemental blend and mechanical alloying techniques. *Mater. Chem. Phys.* **2024**, *312*, 128661. [CrossRef]

Disclaimer/Publisher's Note: The statements, opinions and data contained in all publications are solely those of the individual author(s) and contributor(s) and not of MDPI and/or the editor(s). MDPI and/or the editor(s) disclaim responsibility for any injury to people or property resulting from any ideas, methods, instructions or products referred to in the content.